

## COMPARISON OF TWO CORONAL MAGNETIC FIELD MODELS FOR RECONSTRUCTING A SIGMOIDAL SOLAR ACTIVE REGION WITH CORONAL LOOPS

AIYING DUAN<sup>1,2,4</sup>, CHAOWEI JIANG<sup>3,2,4</sup>, QIANG HU<sup>4,5</sup>, HUAI ZHANG<sup>1</sup>, G. ALLEN GARY<sup>4</sup>, S. T. WU<sup>4</sup>, JINBIN CAO<sup>6</sup>

*Draft version November 5, 2018*

### ABSTRACT

Magnetic field extrapolation is an important tool to study the three-dimensional (3D) solar coronal magnetic field which is difficult to directly measure. Various analytic models and numerical codes exist but their results often drastically differ. Thus a critical comparison of the modeled magnetic field lines with the observed coronal loops is strongly required to establish the credibility of the model. Here we compare two different non-potential extrapolation codes, a non-linear force-free field code (CESE-MHD-NLFFF) and a non-force-free field (NFFF) code in modeling a solar active region (AR) that has a sigmoidal configuration just before a major flare erupted from the region. A 2D coronal-loop tracing and fitting method is employed to study the 3D misalignment angles between the extrapolated magnetic field lines and the EUV loops as imaged by SDO/AIA. It is found that the CESE-MHD-NLFFF code with preprocessed magnetogram performs the best, outputting a field which matches the coronal loops in the AR core imaged in AIA 94 Å with a misalignment angle of  $\sim 10^\circ$ . This suggests that the CESE-MHD-NLFFF code, even without using the information of coronal loops in constraining the magnetic field, performs as good as some coronal-loop forward-fitting models. For the loops as imaged by AIA 171 Å in the outskirts of the AR, all the codes including the potential-field give comparable results of mean misalignment angle ( $\sim 30^\circ$ ). Thus further improvement of the codes is needed for a better reconstruction of the long loops enveloping the core region.

*Subject headings:* Magnetic fields; Magnetohydrodynamics (MHD); Methods: numerical; Sun: corona; Sun: flares

### 1. INTRODUCTION

The observed solar explosive events (e.g., flares and coronal mass ejections) within the corona is attributed to an energy release in the coronal magnetic field. Hence understanding the dynamics and physics of these eruptions is centered on understanding the structure and evolution of the magnetic field. The coronal field can evolve from reconnection and photospheric variations. However, direct measurement of the coronal magnetic field from emissions of the extremely tenuous plasma of the corona by spectropolarimetric methods still proves to be difficult (Lin et al. 2004; Lin 2016). Currently, the routine measurement of solar magnetic field that we can rely on is restricted to only a single layer of solar surface, i.e., the photosphere. Most recently, chromospheric polarimetry is beginning to show promising results, however the height of formation is problematic (Quintero et al. 2017).

Due to the lack of measurement data, the three-dimensional magnetic field in the solar corona is usually “extrapolated” or “reconstructed” in numerical ways from the photosphere surface data based on particular assumptions or models. Such techniques of modeling the coronal magnetic field have been developed (e.g., see review papers of Sakurai 1989; Mc-

Clymont et al. 1997; Solanki et al. 2006; Wiegelmann 2008; Wiegelmann & Sakurai 2012; Régnier 2013). Three magnetic field models often used include the potential field, linear force-free field (LFFF), and nonlinear force-free field (NLFFF). All these models are derived from a basic assumption that the Lorentz force in the corona vanishes in the case of extremely low plasma  $\beta$  ( $\beta$  is the ratio of the plasma pressure to the magnetic pressure) and quasi-static equilibrium of the coronal field. Consequently the electric current  $\mathbf{J} = \nabla \times \mathbf{B}$  must be parallel to the magnetic field, i.e.,  $\mathbf{J} = \alpha \mathbf{B}$  where  $\alpha$  is called the force-free parameter. In the potential field model,  $\alpha = 0$ ; in the LFFF,  $\alpha$  is a constant; and in the NLFFF,  $\alpha$  is variable in space. The earliest models were based on potential field (Altschuler & Newkirk 1969; Sakurai 1982) and LFFF (Seehafer 1978) that are extrapolated from only the data of line-of-sight (LoS) component of the photospheric field since the transverse components were not measured. Now both the LoS and transverse components of the photospheric magnetic field can be measured (e.g., Hoeksema et al. 2014) and information of the electric current passing through the photosphere can derived. Nonlinear force-free field (NLFFF) reconstructions, which are based on the vector magnetograms, are more robust than those earlier models, and employ several numerical schemes (Sakurai 1981; Yang et al. 1986; Wu et al. 1990; Amari et al. 1997; Yan & Sakurai 2000; He & Wang 2006; Wiegelmann & Neukirch 2006; Wheatland 2006; Valori et al. 2010; Jiang & Feng 2012a). Existing NLFFF codes include the optimization method (Wheatland et al. 2000; Wiegelmann 2004; Wiegelmann & Neukirch 2006; Wiegelmann 2008), the magneto-frictional method (Valori et al. 2007, 2010; Guo et al. 2016), the Grad-Rubin method (Amari et al. 2006; Wheatland 2007; Amari et al. 2014), and the MHD-relaxation code based on conservation-element/solution-element space-

duanaiying@ucas.ac.cn, hzhang@ucas.ac.cn, chaowei@hit.edu.cn

<sup>1</sup> Key Laboratory of Computational Geodynamics, University of Chinese Academy of Sciences, Beijing 100049, China

<sup>2</sup> SIGMA Weather Group, State Key Laboratory for Space Weather, National Space Science Center, Chinese Academy of Sciences, Beijing 100190, China

<sup>3</sup> HIT Institute of Space Science and Applied Technology, Shenzhen, 518055, China

<sup>4</sup> Center for Space Plasma and Aeronomic Research, The University of Alabama in Huntsville, Huntsville, AL 35899, USA

<sup>5</sup> Department of Space Science, The University of Alabama in Huntsville, Huntsville, AL 35899, USA

<sup>6</sup> School of Space and Environment, Beihang University, Beijing 100191, China

time scheme (CESE-MHD-NLFFF; [Jiang et al. 2011](#); [Jiang & Feng 2012a, 2013](#)). Now NLFFF models are widely used in the solar physics community for exploring the 3D coronal structure prior to and post solar eruptions and for understanding the influence of the magnetic topology on solar eruptions (e.g., [Guo et al. 2008](#); [Sun et al. 2012](#); [Jiang et al. 2013](#); [Cheng et al. 2014](#); [Liu et al. 2014](#); [Xue et al. 2016](#)).

An alternative to NLFFF extrapolation is an approach based on a magnetic field model of the corona derived from the variational principle of minimum energy dissipation rate ([Hu & Dasgupta 2008](#); [Hu et al. 2008, 2010](#)). The formula governing the coronal magnetic field is more complex, and the solution, expressed as the superposition of three LFFFs (one being potential), is in general not force-free. Such a non-force-free field (NFFF) extrapolation was presented in [Hu & Dasgupta \(2008\)](#) and was shown to be applicable to NLFFF configuration given by [Low & Lou \(1990\)](#) analytic solutions. It was also tested on numerical MHD simulation data for an active region ([Hu et al. 2008](#)). Later it was further developed for practical applications to photospheric vector magnetograms obtained within an active region ([Hu et al. 2010](#)). The implementation of the algorithm is relatively simple and the full code written in Interactive Data Language (IDL) can handle the magnetograms of  $1024 \times 1024$  pixels on a desktop PC. However extensive testing and application of the NFFF algorithm have yet to be performed.

A critical assessment of the reliability of coronal magnetic field extrapolation modeling is to examine the goodness-of-matching of the geometry of the simulated magnetic field lines with that of the observed EUV coronal loops. This is because the plasma emission in the corona reflects the geometry of the invisible magnetic field, as in most parts of the corona the plasma is “frozen” with the magnetic fields. While earlier studies compared theoretical models with observed images in a rather qualitative way, recent studies go into quantitative measurements of the agreement between modeled field lines and observed coronal loop geometries. In an assessment of a variety of popular NLFFF codes for modeling AR 10953, [DeRosa et al. \(2009\)](#) compared the model field lines to 3D trajectories of coronal loops, which are observed stereoscopically by the twin Solar Terrestrial Relations Observatory (STEREO) spacecraft ([Aschwanden et al. 2008](#)). It was found that the misalignment angle between the field lines and the loops amounts to rather large values of  $24^\circ$ – $44^\circ$ , and unexpectedly, none of the examined NLFFF models improved significantly upon the value found for the potential field model. Another method employs a slight variation by measuring the distance between a loop and a projected field line ([Chae & Moon 2005](#); [Lim et al. 2007](#); [Malanushenko et al. 2011](#)). The same idea of a “distance” has also been used in 3D, with STEREO data ([Wiegmann & Neukirch 2002](#)). Without tracing the trajectories of coronal loops, [Wiegmann et al. \(2012\)](#) compared the model field lines with SDO/AIA images by calculating the sum of gradient of the AIA image intensity along each projected field lines, and the result is assumed to reach its minimum if all the field lines are co-aligned with the corresponding loops. The LFFF parameter  $\alpha$ , derived from vector fit to loops has been compared to that derived from a vector magnetogram ([Burnette et al. 2004](#)) providing an additional goodness metric.

Recently, [Gary et al. \(2014b\)](#) developed a new method of deriving the 3D structure of observed 2D coronal loops independent of heliostereoscopy, and suggested that it can determine the matching of extrapolated magnetic fields with coro-

nal loops. In that method, an automated loop recognition scheme (OCCULT-2, [Aschwanden et al. 2013](#)) is first used to extract 2D loop structures from EUV images and then the extracted loops are fitted with 2D cubic Bézier splines that are based on 4 control points ([Gary et al. 2014a](#)). The 2D splines are further extended to 3D with the heights of all 4 control points set as free parameters. The heights are determined by minimizing the misalignment angles of the 3D splines with field lines of a given model of coronal magnetic field, and the resulting 3D splines are regarded as the trajectories of the corresponding coronal loops in 3D. So the image of these loops represents a 2D projection of these 3D structures. Naturally, different magnetic field models will result in different sets of misalignment angles, and a perfect matching model can presumably yield a misalignment angle of zero. Thus this method provides a powerful tool of comparing different magnetic-field models of the corona by using EUV images obtained from one single viewpoint.

Other coronal magnetic field models with forward fitting of coronal loops has been developed for better reproducing the geometry of the loops ([Malanushenko et al. 2012, 2014](#); [Aschwanden 2013a,b](#)). For instance, unlike the traditional NLFFF codes that extrapolate the coronal field from the vector field at the photosphere, the coronal-loop forward-fitting quasi-NLFFF models of [Aschwanden \(2013a\)](#) use only the LoS magnetic field component and the non-potentiality of the field (characterized by the force-free parameter  $\alpha$ ) is determined by minimization of misalignment of the field lines with the traced loops from observed images. [Aschwanden \(2013b\)](#) shows that their code can be applied to either 3D loops determined stereoscopically or simply 2D from LoS observations. In the latter case, the 3D height of the loops is used as a free parameter and a 2D misalignment angle is minimized. The forward-fitting method strongly depends on the recognition of coronal loops from the image, which has been automated by [Aschwanden et al. \(2013\)](#). We should note that even in such forward-fitting of the coronal loops, the misalignment angles of the field line with the loops are significant. For example, the misalignment angle resulted in [Aschwanden \(2013b\)](#) is about  $20^\circ$  in the forward-fitting of TRACE loops.

In this paper, we will evaluate our extrapolation results from the NLFFF (CESE-MHD-NLFFF) and the NFFF codes, by introducing a critical comparison of the modelled magnetic field lines with the coronal loop geometry. In particular, we will employ [Gary et al. \(2014b\)](#)’s method to compute the misalignment angles of the model field lines and identified loops. The target region used in this examination is AR 12158 prior to its major eruption on 2014 September 10, which exhibits a well-shaped sigmoid that indicates a non-potential field. Employing the SDO AIA 94 Angstroms images, we find that one NLFFF solution fits the best (misalignment angle of  $\sim 10^\circ$ ) the AR core loops, but not so well the loops that correspond to large overlying field lines (misalignment angle of  $\sim 30^\circ$ ) near the side boundaries. Our results are similar to those of [DeRosa et al. \(2009\)](#). In addition to the comparison of field lines with coronal loops, we also evaluate quantitatively the extrapolated fields by other means including the magnetic energy, helicity contents, magnetic twist and squashing degree ([Demoulin et al. 1996](#); [Titov et al. 2002](#)). The paper is organized as follows. We first briefly describe the CESE-MHD-NLFFF code and the NFFF code in Sections 2 and 3, respectively. Then in Section 4 we give a short review of the coronal loop tracing and fitting method developed by [Gary et al. \(2014b\)](#). The results of assessing the extrapolated coronal magnetic fields

for AR 12158 are given in Section 5, and finally discussions appear in Section 6.

## 2. THE CESE–MHD–NLFFF CODE

The CESE–MHD–NLFFF code (Jiang & Feng 2013) belongs to the class of MHD relaxation methods. It solves a set of modified zero- $\beta$  MHD equations with frictional force using an advanced conservation-element/solution-element (CESE) spacetime scheme on a non-uniform grid with parallel computing (Jiang et al. 2010). The modified MHD equations are written as

$$\frac{\partial \rho \mathbf{v}}{\partial t} = (\nabla \times \mathbf{B}) \times \mathbf{B} - \nu \rho \nabla^2 \mathbf{v}, \quad \rho = |\mathbf{B}|^2, \quad \frac{\partial \mathbf{B}}{\partial t} = \nabla \times (\mathbf{v} \times \mathbf{B}) \quad (1)$$

where  $\nu$  is the frictional coefficient. The initial condition for the computation sequence is a potential field extrapolated from the vertical component of the vector magnetogram. To drive the evolution of the field, we change the horizontal magnetic components at the bottom boundary gradually until they match the vector magnetogram, after which the system will be relaxed to a new equilibrium. Details of this code can be found in (Jiang & Feng 2012a; Jiang et al. 2012). It is well tested by different benchmarks including the Low & Lou (1990)'s analytic force-free solutions and the Titov & Démoulin (1999)'s magnetic flux rope model, and recently applied to the SDO/HMI vector magnetograms (Jiang & Feng 2013; Jiang et al. 2014). Here we use the code in exactly the same way as Jiang & Feng (2013), without any parameter optimization for the present modeling.

Unlike the coronal field, the photospheric field is not necessarily force-free because of much higher plasma  $\beta$ , thus it is usually required to remove the Lorentz force in the vector magnetogram for a boundary field consistent with the force-free assumption of NLFFF extrapolations (Wiegmann & Neukirch 2006). Meanwhile, smoothing of original magnetogram is needed to reduce the data noise and smooth the very small-scale structures that cannot be properly resolved by the discretized grid. Such process of removing force and smoothing is called preprocessing and here we use the preprocessing code developed by Jiang & Feng (2014). Different from other preprocessing codes (Wiegmann & Neukirch 2006; Fuhrmann et al. 2007, 2011), this code is unique in that it splits the vector magnetogram into a potential field part and a non-potential field part and handles the two parts separately. The potential part, as it is already force-free, only needs smoothing, which is simply performed by taking the data sliced at a plane one pixel (of an HMI magnetogram) above the photosphere from the 3D extrapolated potential field. Then the non-potential part is modified and smoothed by an optimization method to fulfill the constraints of total magnetic force-freeness and torque-freeness. One advantage of using such a splitting is that the preprocessing of the non-potential field part can be guided by the extents of force-freeness and smoothness of the smoothed potential-field part. This is because in the practical computation, particular attention needs to be paid on what extent the force needs to be removed and the smoothing can be performed. In practical computation based on numerical discretization, an accurate satisfaction of force-free constraints is apparently not necessary. Also the extent of the smoothing for the data needs to be carefully determined, if we want to mimic the expansion of the magnetic field from the photosphere to some specific heights. Over-smoothing of the data may smear the basic structures while insufficient smoothing cannot filter the small-

scale noise sufficiently. A careful choice of the weighting factors  $\mu$  is required to deal with these problems. In Jiang & Feng (2014) the values of force-freeness and smoothness calculated from the preprocessed potential-field part are used as a reference, and the target magnetogram is required to have the same level of force-freeness and smoothness as its potential part in numerical precision. It is found that these requirements can restrict well the free parameters, i.e., the weighting factors  $\mu$  in the optimization function.

## 3. THE NON-FORCE-FREE EXTRAPOLATION CODE

The non-force-free field is governed by the following equation (Hu & Dasgupta 2008; Hu et al. 2010):

$$\nabla \times \nabla \times \nabla \times \mathbf{B} + a \nabla \times \nabla \times \mathbf{B} + b \nabla \times \mathbf{B} = 0. \quad (2)$$

One solution is written  $\mathbf{B} = \mathbf{B}_1 + \mathbf{B}_2 + \mathbf{B}_3$ , where each sub-field  $\mathbf{B}_i$  satisfies the standard LFFF equation with distinct parameters  $\alpha_i, i = 1, 2, 3$ , such that  $a = -(\alpha_1 + \alpha_3)$  and  $b = \alpha_1 \alpha_3$ . To obtain a solution of this form, taking advantage of the relatively simple solutions to LFFFs, it turns out that  $\alpha_2 = 0$ , and  $\alpha_1 \neq \alpha_3 \neq 0$ . Therefore, one of the sub-fields,  $\mathbf{B}_2$ , becomes potential field solution for the boundary conditions.

For completeness, we give below a brief description of the algorithm of deriving an NFFF solution to equation (2) via the superposition of three LFFFs of distinct  $\alpha$  parameters. It can be shown that the result is the following equation,

$$\begin{pmatrix} \mathbf{B}_1 \\ \mathbf{B}_2 \\ \mathbf{B}_3 \end{pmatrix} = \mathcal{V}^{-1} \begin{pmatrix} \mathbf{B} \\ \nabla \times \mathbf{B} \\ \nabla \times \nabla \times \mathbf{B} \end{pmatrix}. \quad (3)$$

Here the matrix  $\mathcal{V}$  is composed of elements  $\alpha_j^{i-1}, i, j = 1, 2, 3$ , which is a Vandermonde matrix and is guaranteed invertible as long as the  $\alpha$ 's are distinct (Hu & Dasgupta 2008). Therefore each LFF sub-field can be solved for the known  $\alpha$  parameter, and the given normal boundary condition by using a standard LFFF solver (Alissandrakis 1981). Ideally the bottom boundary condition, as given by the right-hand side of Equation (3), has to be derived by utilizing two or more than two layers of vector magnetograms since the vertical gradient as well as the transverse gradients of magnetic field have to be calculated. If multiple layer vector magnetograms are available, then the right-hand side of Equation (3) can provide the boundary conditions (vertical components) for each sub-field, given known  $\alpha$  parameters. So the optimal pair of  $(\alpha_1, \alpha_3)$  parameters, while keeping  $\alpha_2 \equiv 0$ , is determined by a trial-and-error process by finding a pair which minimizes the average deviation between the observed  $(\mathbf{B}_t)$  and the calculated  $(\mathbf{b}_t)$  transverse field, as indicated by the following metric (Hu & Dasgupta 2008):

$$E_n = \sum_{i=1}^M |\mathbf{B}_{t,i} - \mathbf{b}_{t,i}| / \sum_{i=1}^M |\mathbf{B}_{t,i}|. \quad (4)$$

However, since most vector magnetograms are only available on the photosphere, which only allows for an evaluation of  $(\nabla \times \mathbf{B})_z$ , the boundary conditions for each sub-field cannot be provided by the third-order system of Equation (3). An algorithm was devised by Hu et al. (2010) to work with the single layer vector magnetogram by adding an additional round of iteration over successive correction to the potential sub-field  $\mathbf{B}_2$ . Starting with an initial guess, e.g., the simplest being  $\mathbf{B}_2 = 0$ , the system of Equation (3) is reduced to 2nd-order which allows for the determination of boundary conditions

for  $\mathbf{B}_1$  and  $\mathbf{B}_3$ , and thus the normal trial-and-error process as described above. If the resulting minimum  $E_n$  value is not satisfactory, then a corrector potential field to  $\mathbf{B}_2$  is derived from the difference transverse field, i.e.,  $\mathbf{B}_t - \mathbf{b}_t$ , and added to the previous  $\mathbf{B}_2$ , in anticipation of improved match between the transverse fields, as measured by  $E_n$ . The positive effect of such successive corrections is generally demonstrated by a monotonic decrease in  $E_n$  from an initial value around 1.0 to less than 0.3, after 10,000 steps (Hu et al. 2010).

The algorithm relies on the implementation of fast calculations of the LFFFs including the potential field, such as the classic algorithm of Alessandrakis via Fast Fourier Transform (FFT) for an active region in a Cartesian box with periodic boundary conditions. It is highly desirable to extend the scheme to the whole solar sphere, by taking advantage of the recently developed fast algorithm of Jiang & Feng (2012b) for global LFFF (including potential) extrapolation based on FFT as well. This extension also overcomes the limitation of flux imbalance intrinsic to the LFFF within a finite AR. This would contribute to the errors in our current NFFF extrapolation of AR magnetic field, which is based on LFFF solutions.

#### 4. CORONAL LOOP TRACING AND FITTING

Here we briefly review the procedures of tracing and fitting the coronal loops developed by Gary et al. (2014b). First, an automated loop recognition scheme (the code OCCULT-2) is employed to trace the loop structures from the EUV images taken by SDO/AIA in 171 Å. The OCCULT-2 code was developed by Aschwanden et al. (2013) and is included in the SolarSoftWare (SSW), named as “looptracing\_auto4.pro”, and here we use the version dated 8-Dec-2015. The code provides a group of input parameters to control the tracing, which are given here respectively following Aschwanden et al. (2014): the low-pass-filter constant  $n_{\text{sm1}} = 5$ , the minimum loop curvature radius  $r_{\text{min}} = 30$ , the minimum loop length  $l_{\text{min}} = 20$ ,  $n_{\text{loop}} = 50$  and the base level factor  $q_{\text{med}} = 5$ . The code outputs a number of 2D curves corresponding to the 2D loop identified from the EUV images. Then each of the traced 2D loops is fitted by a 2D cubic Bézier spline, which is defined by four control points as (Gary et al. 2014a,b)

$$\begin{aligned} \mathbf{R}(u) = & [(1-u)^3 x_1 + 3u(1-u)^2 x_2 + 3u^2(1-u)x_3 + u^3 x_4, \\ & (1-u)^3 y_1 + 3u(1-u)^2 y_2 + 3u^2(1-u)y_3 + u^3 y_4, \\ & (1-u)^3 z_1 + 3u(1-u)^2 z_2 + 3u^2(1-u)z_3 + u^3 z_4] \end{aligned} \quad (5)$$

where  $u \in [0, 1]$  is a parameter along the curve,  $(x_j, y_j, z_j)$  with  $j = 1, 2, 3, 4$  are the coordinates of the four control points, and here  $z_j = 0$  and so  $z = 0$  as for a 2D curve. The fitting is realized by minimizing the RMS distances of 10 equally-spaced points along the loop curve and the Bézier spline. It was proven that generally there is no need to use a higher-order curve than cubic Bézier curve (of 3rd order), which can sufficiently fit the EUV loops (Gary et al. 2014a,b). After this, the 2D Bézier splines are extended to 3D by determining the four non-zero  $z_j$  coordinates for which the curve (Equation 5) has minimal misalignment angle with the field vector along it. In particular, at a given point  $\mathbf{R}$  of a Bézier curve, the misalignment angle  $\mu(\mathbf{R})$  between the direction of the 3D spline (or the 3D coronal loop)  $\mathbf{L}(\mathbf{R})$  and the magnetic field model  $\mathbf{B}(\mathbf{R})$  at the same point is defined as

$$\mu(\mathbf{R}) = \arccos \left[ \frac{\mathbf{B}(\mathbf{R}) \cdot \mathbf{L}(\mathbf{R})}{|\mathbf{B}(\mathbf{R})| |\mathbf{L}(\mathbf{R})|} \right], \quad (6)$$

Thus for a single loop, a mean misalignment angle can be defined by

$$\xi = \frac{1}{\Gamma} \sum_{k=1}^{\Gamma} \mu(\mathbf{R}_k), \quad (7)$$

where  $k$  is node index of the curve, and here we use an evenly-spaced 100 points ( $\Gamma = 100$ ) along the loop length. As  $\xi$  is a function of the four altitudes  $z_j$ , the best-fit altitudes  $z_j^*$  are determined by minimizing  $\xi$ . After applying the minimization program to all the loops, statistical assessments of misalignment of the model field lines and loops can then be performed.

#### 5. RESULTS

AR 12158 on 2014 September 10 is selected as our target of study because of its clear sigmoidal configuration imaged by SDO/AIA in 171 Å channel as well as its near disk-center location. Figure 1 shows that AR 12158 was passing the central meridian on 2014 September 10, and moreover, the region appears to be isolated from neighboring ARs, although there are relatively long coronal loops reaching far from the core region. An eruptive flare of X1.6 class occurred in the core of this region, which began at 17:21 UT, reached its peak at 17:45 UT, and ended at 18:20 UT. This sigmoid and its flare have been studied by several authors. From observations of SDO/AIA and interface region imaging spectrograph (IRIS), Cheng et al. (2015) suggested that prior to the major eruption a magnetic flux rope is under formation by tether-cutting reconnection (Moore et al. 2001) between two groups of sheared arcades driven by the shearing and converging flows in the photosphere near the polarity inversion line. Li & Zhang (2015) reported slipping reconnection of flaring loop during the flare process, which was also carefully studied by Dudík et al. (2016) in the context of the 3D standard flare model (Aulanier et al. 2012; Janvier et al. 2013). NLFFF extrapolation of the coronal magnetic field about 2 hours before the flare has been carried out by Zhao et al. (2016) using a Grad-Rubin code implemented in spherical coordinates (Gilchrist & Wheatland 2014). By computing a map of the magnetic field squashing factor (Titov & Démoulin 1999), Zhao et al. (2016) suggested that the locations of QSLs agrees to some extent with the observed flare ribbons, which are predicted by the 3D standard flare model. They found a strongly twisted and complex magnetic flux rope in the extrapolation, the shape of which, however, is not seen in AIA images.

Here we perform extrapolations of the coronal magnetic field immediately before the X-class flare onset. Specifically we use the HMI vector magnetogram at 17:00 UT on September 10, and the extrapolations are to be compared with the AIA observations at 17:10 UT. The reason for selecting AIA observations at 17:10 UT is that the sigmoid-shaped emission appears to be most distinctive in the 94 Å channel when we inspect the AIA images before the flare beginning time of 17:21 UT (see Figure 2). As can be seen in Figure 2, the loop-tracing code OCCULT-2 identifies a bundle of loops forming an inverse S shape, which looks most apparent at the selected time. The Space weather HMI Active Region Patches (SHARP) vector magnetogram data product ‘hmi.sharp\_cea\_720s’ (Hoeksema et al. 2014; Bobra et al. 2014) is used for our extrapolation. It includes vector magnetograms projected and re-mapped onto the cylindrical equal area (CEA Snyder 1987) Cartesian coordinate system centered on the tracked AR, which is well-suited for the Cartesian

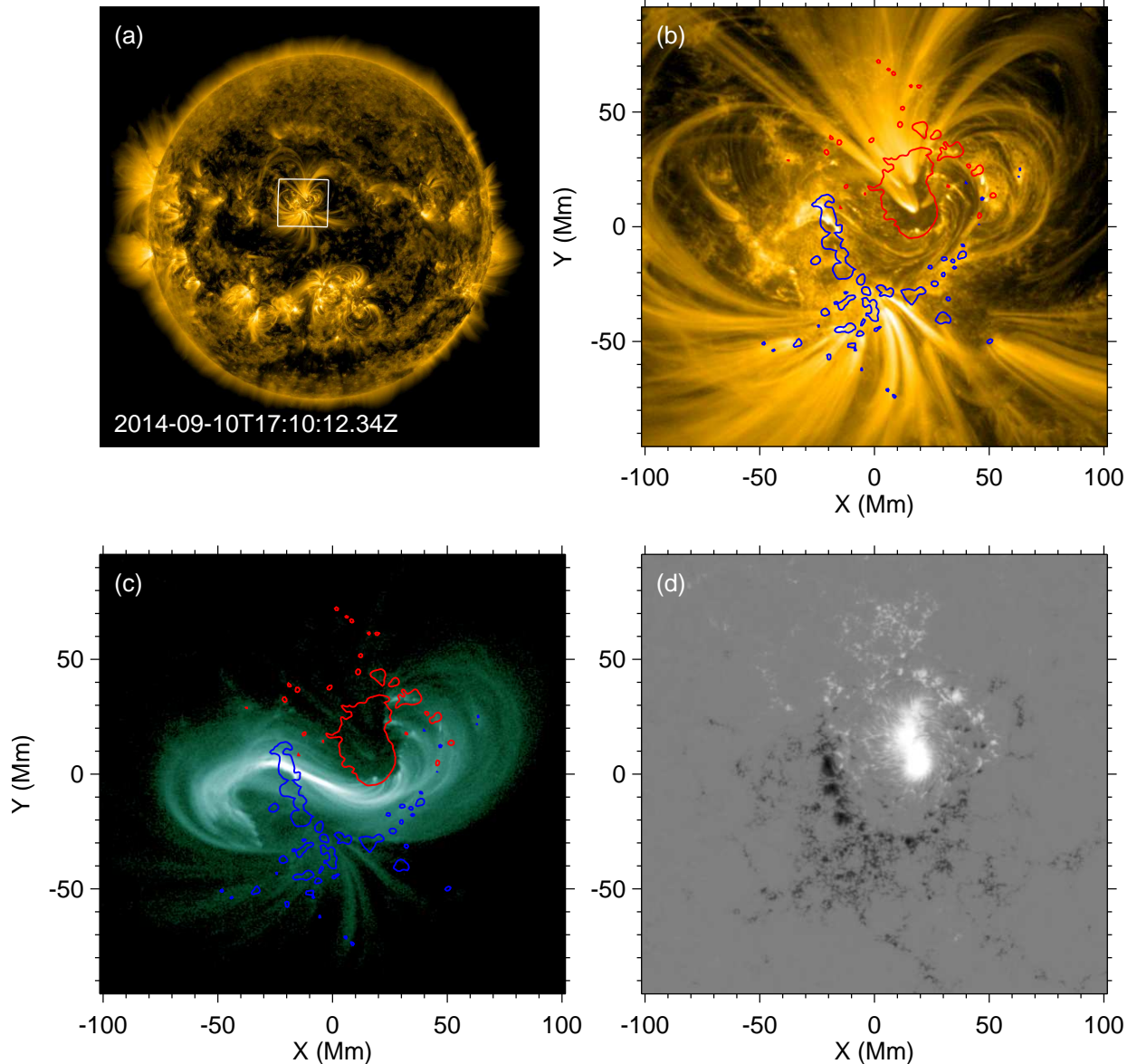


FIG. 1.— Observations of AR 12158 at the time 17:10 UT on 2014 September 10. (a) AIA 171 Å full-disk image with location of AR 12158 marked by the box. (b) Close view of the boxed region. (c) Same as (b) but in AIA 94 Å channel. (d) SHARP CEA remapped LoS magnetogram.

version of our code. For comparing the coronal loops with the modeled field, we realign the AIA images using the same CEA remapping to assure that the AIA images are co-aligned with the magnetogram. We note this is reasonable only when the target region is located near the disk center and should be small enough, such that the solar radial direction is nearly co-aligned with the line of sight and the 2D loops in the AIA image correspond to projection of 3D loops along the radial direction. Otherwise, comparison of the magnetic field lines with traced loops from EUV images should be performed directly in spherical geometry (Aschwanden et al. 2014) using a spherical version of the Gary et al. (2014b)’s loop-fitting code, and thus extrapolation in spherical coordinates is required (e.g., Jiang et al. 2012; Tadesse et al. 2014; Gilchrist & Wheatland 2014).

For the given SHARP vector magnetogram at the selected time, we apply three magnetic field models with different numerical method and different boundary conditions. The first

one (NLFFF1) is CESE–MHD–NLFFF modeling using the original vector magnetogram. The second one (NLFFF2) is CESE–MHD–NLFFF with the preprocessed magnetogram. The third model is NFFF extrapolation, which also uses the vector magnetogram without preprocessing as in NLFFF1. All the extrapolations use the same resolution of 1 arcsec, and the results are compared within the same effective volume of  $282 \times 266 \times 200 \text{ arcsec}^3$ .

In the following sections, we assess and compare the magnetic field models in different ways including the magnitude of the Lorentz force and the quality of divergence-freeness, the magnetic configuration and topology features by computing the magnetic field lines and squashing degree, misalignment of the magnetic field lines with the traced loops, and finally the magnetic energy and helicity content of the fields.

### 5.1. Lorentz force and magnetic field divergence

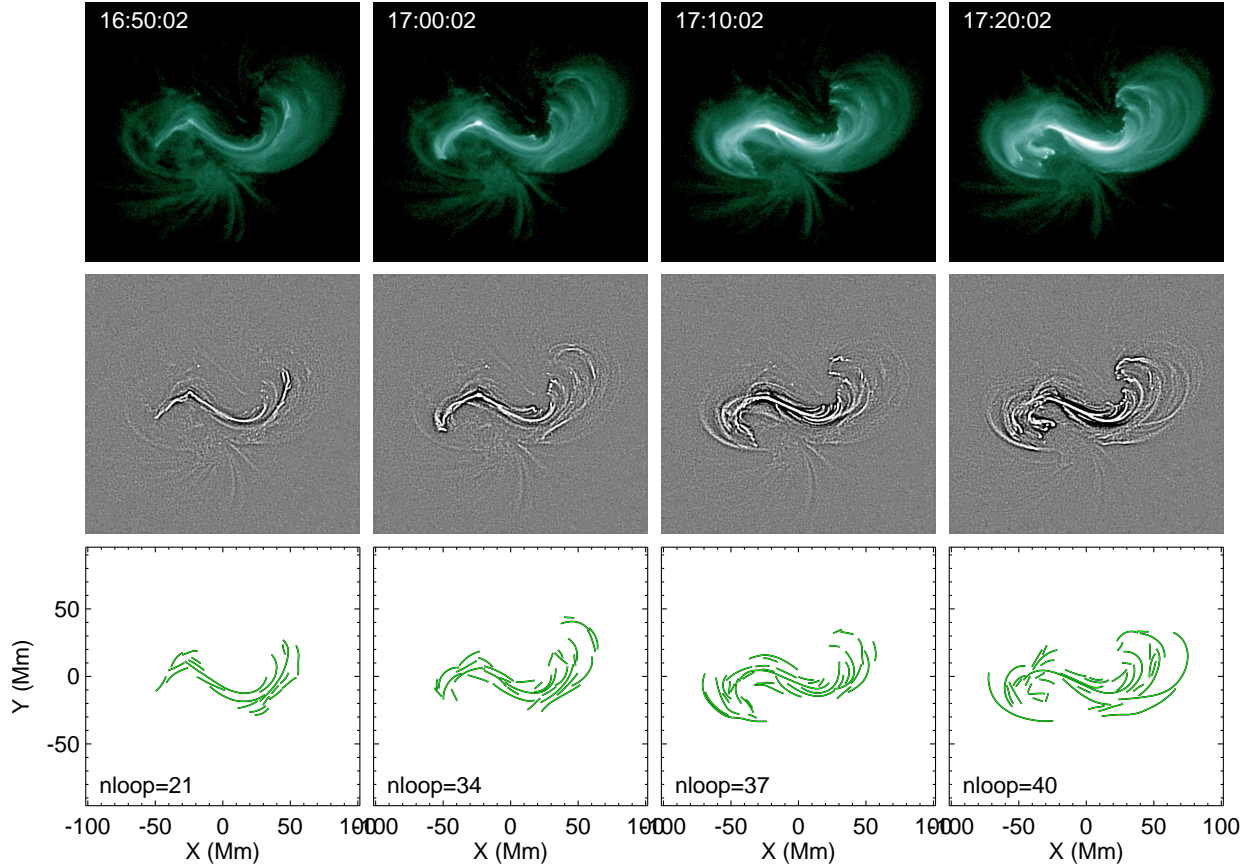


FIG. 2.— Top: AIA 94 Å images of the sigmoid around the flare time. Middle: Same AIA data as the top but is bandpass filtered with a low-pass-filter boxcar of  $n_{\text{rmsm1}} = 5$  pixels and a high-pass-filter boxcar of  $n_{\text{sm2}} = 7$  pixels. Bottom: Automated loop tracing of the bandpass-filtered images using the code OCCULT-2.

To check the quality of force-freeness and divergence-freeness of the reconstructed fields, two metrics are routinely used (e.g., Schrijver et al. 2006; DeRosa et al. 2009; Jiang & Feng 2013): the mean sine of the angle between current  $\mathbf{J}$  and  $\mathbf{B}$  weighted by  $J$ , named as  $\text{CWsin}$  and defined by

$$\text{CWsin} \equiv \frac{\int_V J \sigma dV}{\int_V J dV}; \quad \sigma = \frac{|\mathbf{J} \times \mathbf{B}|}{JB}, \quad (8)$$

where  $B = |\mathbf{B}|$ ,  $J = |\mathbf{J}|$  and  $V$  is the computational volume; and a normalized divergence error measured by

$$\langle |f_i| \rangle = \frac{1}{V} \int_V \frac{\nabla \cdot \mathbf{B}}{6B/\Delta x} dV. \quad (9)$$

These two metrics are equal to zero for an exact or a perfect force-free field; hence, the smaller the metrics are, the better the extrapolation is for a force-free field. However, for a field with very small current, the  $\text{CWsin}$  does not necessarily give a reliable or meaningful value because of random numerical errors. As an example, value of  $\text{CWsin}$  could be close to 1 for a potential field solution computed by Green’s function method or other numerical realization. The reason is that the numerical finite difference, used for computing the current  $\mathbf{J} = \nabla \times \mathbf{B}$  from  $\mathbf{B}$ , gives small but finite currents, whose directions are randomly from  $0^\circ$  to  $180^\circ$ , thus the angle between  $\mathbf{J}$  and  $\mathbf{B}$  should have an average value of  $\sim 90^\circ$ . Consequently, the distribution of  $\text{CWsin}$  for a NLFFF is ‘contaminated’ by this if a substantial portion of the volume is current-free. The issue has been previously noted (Jiang & Feng 2012a; Malanushenko et al. 2014). Small-scale struc-

tures (mainly in the weak field regions) in the solar magnetograms, as are not sufficiently resolved, also might increase the value of  $\text{CWsin}$ . This is because in these regions, although the magnetic field strength is small, the derived current by numerical difference might not be small and their directions are often random. It seems to explain why usually many NLFFF extrapolations from real magnetograms give  $\text{CWsin}$  values, for example,  $\sim 0.30$  (DeRosa et al. 2009), which is much larger than results of benchmark tests with ‘idealized magnetogram’ (which are  $\sim 0.1$  or even smaller, see Jiang & Feng 2012a). As demonstrated by Jiang & Feng (2013), the  $\text{CWsin}$  value decreases significantly in the regions of AR core or with strong currents where the influence of random errors is suppressed.

Metrics of measuring the force-freeness and divergence-freeness can be defined in another way by analyzing the residual force in extrapolations (Jiang & Feng 2012a; Malanushenko et al. 2014). We note that the residual force actually consists of two parts, the Lorentz force and a force induced by non-zero divergence of the field. This is because a nonzero  $\nabla \cdot \mathbf{B}$  can be assumed as being a magnetic monopole, and analogous to a charge in electric field, it introduces a force  $\mathbf{F} = \mathbf{B} \nabla \cdot \mathbf{B}$  parallel to the field line (Dellar 2001). Of course this force is un-physical and only results from numerical error. To define a reference value for these forces, we decompose the Lorentz force,  $(\nabla \times \mathbf{B}) \times \mathbf{B}$ , into two components,

$$(\nabla \times \mathbf{B}) \times \mathbf{B} = (\mathbf{B} \cdot \nabla) \mathbf{B} - \nabla(B^2/2) \quad (10)$$

where the two terms on the right hand side are called, respectively, magnetic tension force and magnetic pressure force.

These two components should be balanced in a force-free field, but each is in general nonzero except in an uniform magnetic field. Thus a metric of Lorentz force-freeness can be defined by the average ratio of the Lorentz force to the sum of the magnitudes of the two component forces, namely,

$$E_{\nabla \times \mathbf{B}} = \frac{1}{V} \int_V \frac{|\mathbf{B} \times (\nabla \times \mathbf{B})|}{|\mathbf{B} \cdot \nabla \mathbf{B}| + |\nabla(B^2/2)|} dV. \quad (11)$$

This is identical to Equation (10) of Malanushenko et al. (2014), and is similar to Equation (26) of Jiang & Feng (2012a) which only used the magnitude of magnetic-pressure force as denominator. Similarly, we measure the magnitude of the other force  $\mathbf{B} \nabla \cdot \mathbf{B}$  by

$$E_{\nabla \cdot \mathbf{B}} = \frac{1}{V} \int_V \frac{|\mathbf{B}(\nabla \cdot \mathbf{B})|}{|\mathbf{B} \cdot \nabla \mathbf{B}| + |\nabla(B^2/2)|} dV. \quad (12)$$

These two metrics  $E_{\nabla \times \mathbf{B}}$  and  $E_{\nabla \cdot \mathbf{B}}$  are meaningful in particular if the extrapolation field is used as initial condition for MHD simulations (e.g., Jiang et al. 2013; Kliem et al. 2013; Amari et al. 2014; Inoue et al. 2014), because they directly reflect the influence of the residual force on the numerical MHD system. Thus we recommend to check these two metrics before using NLFFF (or any other) solutions to initialize MHD code, and examine carefully the related influence. For a typical plasma  $\beta \sim 0.01$  in the lower corona (Gary 2001), the residual force that can be balanced by the gas pressure should be accordingly  $\sim 0.01$  of the magnetic-pressure force, thus the two metrics should be as small as  $\sim 0.01$  if the residual force can be considered as negligible.

TABLE 1  
METRICS OF FORCE-FREENESS AND DIVERGENCE-FREENESS FOR THE THREE EXTRAPOLATION MODELS AND THE POTENTIAL FIELD MODEL

Model	CWsin	$\langle  f_i  \rangle$	$E_{\nabla \times \mathbf{B}}$	$E_{\nabla \cdot \mathbf{B}}$
NLFFF1	0.40	$4.6 \times 10^{-4}$	0.22	$4.3 \times 10^{-2}$
NLFFF2	0.32	$3.9 \times 10^{-4}$	0.16	$3.6 \times 10^{-2}$
NFFF	0.80	$1.2 \times 10^{-5}$	0.31	$1.4 \times 10^{-4}$
Potential	0.86	$6.0 \times 10^{-6}$	$1.2 \times 10^{-4}$	$2.5 \times 10^{-4}$

The results for the aforementioned metrics are given in Table 1 for all the three extrapolation models as well as a potential field model that matches the magnetogram. From the results, we find that all the metrics decrease from NLFFF models 1 to 2, showing that the NLFFF extrapolations are improved by the preprocessing of the vector magnetogram, and their values are close to the results in our previous work for extrapolation of AR 11158 and AR 11283 (Jiang & Feng 2013), suggesting that the performance of CESE-MHD-NLFFF code is not sensitive to different ARs. The divergence metric  $\langle |f_i| \rangle$  is on the order of  $10^{-4}$ , which is consistent with previous results (e.g., Metcalf et al. 2008; Valori et al. 2013; DeRosa et al. 2015). The value is smaller by one order for the NFFF as it is a superposition of three constant-alpha fields, and it is close to the value for the potential field model. Comparing  $E_{\nabla \cdot \mathbf{B}}$  and  $E_{\nabla \times \mathbf{B}}$  shows that the force induced by the divergence are significantly smaller than the Lorentz force. We note that the residual force as measured by these two metrics is larger than what can be neglected if the extrapolated field is input to an MHD model as a force-free state. On the other hand, the Lorentz force as measured by both CWsin and  $E_{\nabla \times \mathbf{B}}$  is much larger in the NFFF extrapolation than the NLFFFs, as it should be, although the numerical and measure-

ment uncertainties would still contribute to this value as described earlier. The divergence-freeness condition is fulfilled much better in the NFFF solution, which is close to the values of that for the potential field model. This is because the NFFF solution is the sum of three LFFF's for which the divergence is guaranteed to be as small as the numerical scheme would allow. Finally we note that CWsin for the potential field is indeed close to 1, which fails to indicate the force-freeness of a current-free field, as we have discussed, while the  $E_{\nabla \times \mathbf{B}}$  gives a reasonable value of  $\sim 10^{-4}$ , which is as small as the value of  $E_{\nabla \cdot \mathbf{B}}$ .

## 5.2. Magnetic field lines, current, and topology

In Figure 3 we compare the magnetic lines, electric current distributions, and magnetic topology for three magnetic fields. The columns from left to right are respectively for NLFFF1, NLFFF2, and NFFF. The magnetic field lines are sampled and shown in the first row of the figure. Each field line is color-coded by the mean value of the electric current density ( $J = |\nabla \times \mathbf{B}|$  in G arcsec $^{-1}$ ) along the line. The second row of the figure shows a vertical integration of the current density ( $\int_z J dz$  with unit of G). Overall an inverse-S shape of strong current can be seen, especially in the NLFFFs, which is very roughly consistent with the AIA 94 Å image (Figure 1c). The strongest current are associated with the magnetic field lines in the core region, which corresponds to the brightest loops in AIA 94 Å image. The magnetic field lines of all the models here are mostly sheared arcades rather than fully S shapes, and show no presence of the strongly twisted magnetic flux rope that is found in the extrapolation by Zhao et al. (2016). Our results seem to agree with the observations of AIA, from which the loop tracing code identifies approximately formed S-shaped loops. From a visual inspection of the magnetic field lines of the models, it appears that in the core region the NLFFFs possess stronger shear than the NFFF, contrarily, in the enveloping field region, the latter has slightly stronger sheared field lines than the former ones. Consistently, the current distribution of the NFFF is more diffused than that of the NLFFF models.

To further compare the magnetic topology, we compute the magnetic squashing degree at the bottom surface. The squashing degree, or  $Q$  factor, is a quantity measuring shape distortions of elemental flux tubes based on the field-line mapping (Demoulin et al. 1996; Titov et al. 2002). Specifically, starting at footpoint  $(x, y)$ , the other footpoint of a closed magnetic field line is denoted by  $(X(x, y), Y(x, y))$  for a given coronal field model. Then  $Q(x, y)$  is given by

$$Q = \frac{a^2 + b^2 + c^2 + d^2}{|ad - bc|} \quad (13)$$

where

$$a = \frac{\partial X}{\partial x}, \quad b = \frac{\partial X}{\partial y}, \quad c = \frac{\partial Y}{\partial x}, \quad d = \frac{\partial Y}{\partial y}. \quad (14)$$

Thus a small value of  $Q$  indicates that a infinitesimal circle at one foot-point is mapped to a circle at the other foot-point, while a very high value (e.g.,  $> 100$ ) indicates extreme distortion of the circle, which indicates steep gradient of the field-line mapping that occurs in magnetic quasi-separatrix layers (QSLs). Thus the  $Q$  factor is useful for searching for important topological structures like separatrices and QSLs. They prove to be relevant to the studies of reconnection sites in the corona and thus physics of flares. For computing  $Q$ , we use

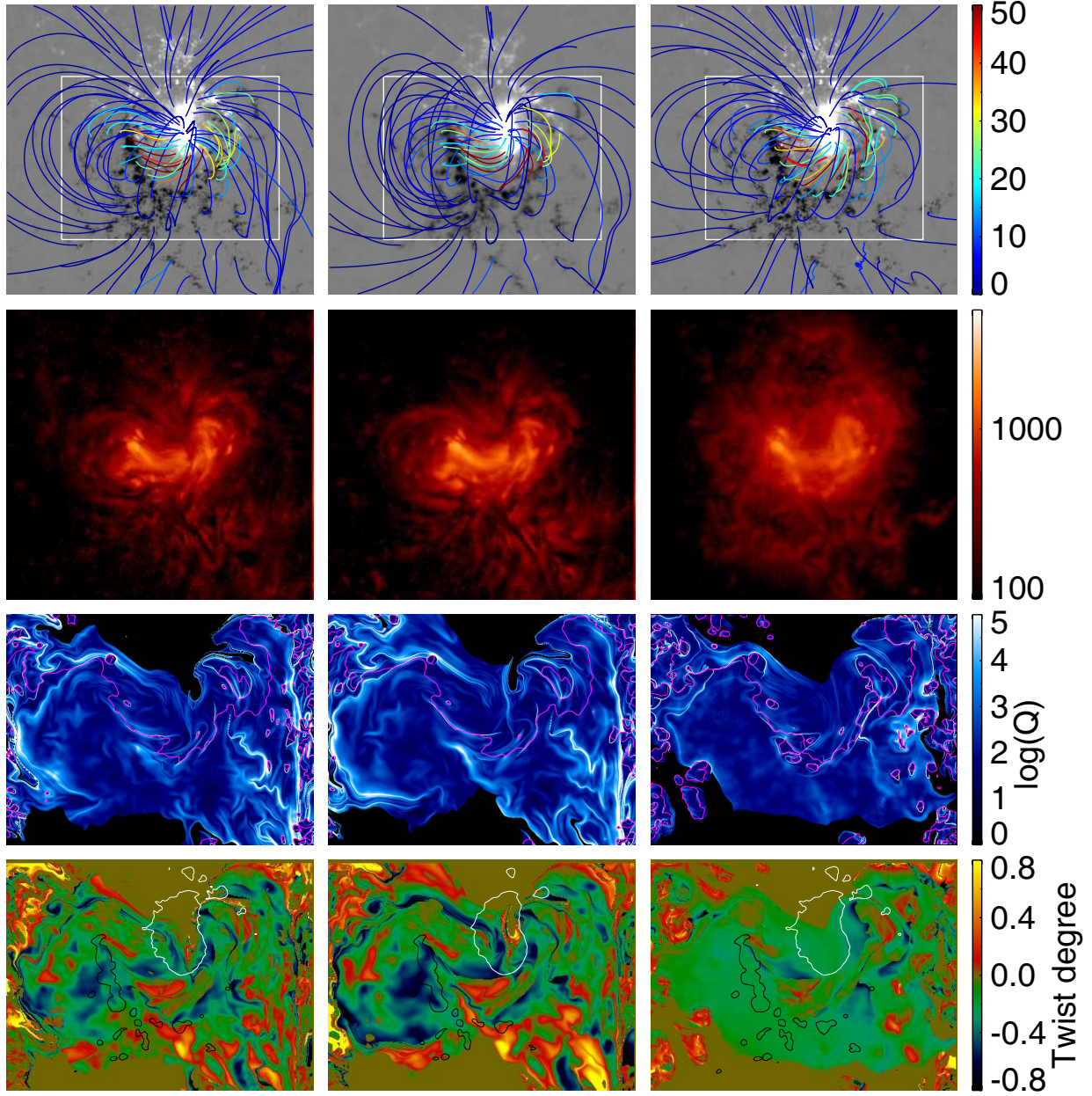


FIG. 3.— Comparison of the three extrapolation models (columns from left to right corresponding to NLFFF1, NLFFF2 and NFFF, respectively) by magnetic field lines, electric current distributions, magnetic squashing degree and twist degree (rows from top to bottom). In the plot of magnetic field line is color-coded by the mean value of the electric current density ( $J = |\nabla \times \mathbf{B}|$  with unit of  $\text{G arcsec}^{-1}$ ) along the line; the backgrounds show the map of  $B_z$ . The current distribution is shown by the vertical integration of the current density ( $\int_z J dz$  with unit of G). The distributions of the magnetic squashing degree  $\log(Q)$  and the twist degree are computed at a horizontal slice one pixel above the bottom surface of the extrapolation box. Their field of view is denoted by the white box in the top panels.

the approach recently proposed by [Pariat & Démoulin \(2012\)](#), which is computationally efficient and can be used to compute  $Q$  inside the 3D domain. The third row of Figure 3 shows the maps of  $Q$  factor. Comparing these three models, we find limited difference between them, and there appears to be no well-shaped QSL defining the boundary of the shear core and the enveloping flux.

In the last row of Figure 3 we show the map of twist ( $T_n$ ) of magnetic field lines (e.g., [Inoue et al. 2011](#); [Liu et al. 2016](#)), which is defined by

$$T_n = \frac{1}{4\pi} \int_L \frac{(\nabla \times \mathbf{B}) \cdot \mathbf{B}}{B^2} dl. \quad (15)$$

where the integral is taken along each closed field line. The magnetic twist  $T_n$  measures number of turns two infinitesimally close field lines make about each other ([Berger & Prior 2006](#)). Both signs of twist are seen in the whole region, and the majority of the core field has a negative value of twist, i.e., a left-handed twisting, and with a relatively small value  $T_n \leq 1$ . This is consistent with the absence of strongly-twisted flux rope in the models. Comparison of the two NLFFF models shows that the preprocessing also results in clear increase of the magnetic twist. The non-force-free model gives a much more weakly twisted field than the NLFFF models, and the distribution of twist degree appears much more even. A fur-

ther study of the magnetic topology and distribution of twist degree and their relation with the eruption is left to a future paper.

### 5.3. Misalignment of the magnetic field lines and AIA loops

Now we report the results of loop fitting to the magnetic field models as described in Section 4. Here we apply the procedures of Gary et al. (2014b) to two AIA channels, i.e., 94 Å and 171 Å, which represent two separate features of the AR field. The 94 Å shows loops at the AR core that are presumably associated with significantly non-potential magnetic field, and they are usually compact and short, while the 171 Å loops correspond to the enveloping field that is often close to a potential state. As described in Section 4, the OCCULT-2 traced loops from the AIA images are first fitted by 2D 4-point Bézier splines. The results are shown in Figure 4. As can be seen, although the 4-point Bézier fitting is previously only applied to AIA 171 Å loops, here it works also pretty well for the AIA 94 Å loops, some of which exhibit slightly S shapes. Then, using the method described in Section 4, the Bézier splines (or loops) are extended to 3D by minimizing the misalignment angle between the loops and the 3D magnetic field. Figures 5 and 6 give the results of such a minimization of the misalignment angle for each loop, and the different panels in the figures are for different extrapolation models of magnetic field. For convenience of comparison, the loops are shown by the thick curves color-coded by value of corresponding misalignment angle with the magnetic field, and for each loop, a magnetic field line is traced passing through the mid-point of the loop, which are shown by the thin curves. The median and mean values of all the misalignment angles for each magnetic field model are also shown in the figures.

We find that model NLFFF2 gives the best results in fitting to the AIA 94 Å loops as it has the smallest values for both the median and mean of the misalignment angles. For the AIA 171 Å loops, NLFFF2 also gives the smallest median value, while the smallest average value is given by the potential field model. Comparing the results for the two AIA channels, we notice that the fitting of the modeled field lines to loops is much better for the 94 Å than for 171 Å. In particular in the best model (NLFFF2), the misalignment angles for the 94 Å loops, which have median value of  $\sim 10^\circ$  and mean value of  $\sim 15^\circ$ , are less than half of those for the 171 Å loops ( $\sim 30^\circ$ ). For 94 Å loops, all the non-potential models give significantly smaller value of misalignment than the potential field model, which confirms that these loops are associated with magnetic field of significant non-potentiality. Improvement from preprocessing of the magnetogram for NLFFF extrapolation is also confirmed by the decrease of the misalignment angles.

It is worthy noting that our best results for the AIA 94 Å loops are on the order of the results using coronal loop forward-fitting NLFFF code shown in Aschwanden (2013b), who found that the 3D misalignment angle amounts to an average value of  $19^\circ \pm 3^\circ$  for their studied ARs. However, for the 171 Å loops, our extrapolation models perform, at the best, only close to the potential field model (with misalignment of  $\sim 30^\circ$ ). Such value is comparable to the misalignment angles ( $24^\circ - 44^\circ$ ) as resulted from a comparison of various NLFFF models for AR 10953 by DeRosa et al. (2009), who also found that those NLFFF models perform no better than potential model. The NLFFF1 without preprocess-

ing gives even larger misalignment angle than the potential model, and it is slightly improved from the preprocessing. The different values for 94 Å and 171 Å show that the CESE-MHD-NLFFF code can reconstruct much more reliably the AR core field (which is significantly non-potential) than the envelope field (which is presumably close to potential). The large misalignment of the extrapolated field with the 171 Å loops is because the field lines corresponding to the long loops do not relax sufficiently during the MHD-relaxation process. Since in the code the relaxation speed is uniform and the relaxation time is thus proportional to the field line length, the long field lines need more time to relax than the short ones. Moreover, the long field lines often extend close to or reach side and top boundaries of the computational volume and are subject to the boundary effects, as all these boundaries are fixed with the initial potential field (however note that the computational volume is larger than the field-of-view of the magnetogram). Another factor which might be partially responsible for this effect is the departure from the Cartesian coordinates assumption further away from the core. Thus a further optimization of the relaxation process with realization of spherical geometry is needed for a better reconstruction of the enveloping field.

TABLE 2  
MAGNETIC FLUX, ENERGY CONTENTS AND RELATIVE HELICITY OF THE EXTRAPOLATION MODELS. UNITS ARE RESPECTIVELY,  $10^{22}$  MX FOR MAGNETIC FLUX,  $10^{32}$  ERG FOR MAGNETIC ENERGY, AND  $10^{43}$  MX<sup>2</sup> FOR MAGNETIC HELICITY.

Model	$\Phi$	$E_{\text{tot}}$	$E_{\text{pot}}$	$E_{\text{free}}$	$E_{\text{free}}/E_{\text{pot}}$	$H$	$H/\Phi^2$
NLFFF1	3.41	11.5	11.7	-0.18	-1.5%	-1.60	$-1.38 \times 10^{-2}$
NLFFF2	3.18	11.1	10.0	1.10	10.9%	-2.03	$-2.00 \times 10^{-2}$
NFFF	3.41	14.8	11.8	3.02	25.6%	-2.36	$-2.04 \times 10^{-2}$

### 5.4. Magnetic energy and helicity

In Table 2 we list the magnetic energy contents and relative helicity for the extrapolation solutions. Both the total magnetic energy  $E_{\text{tot}}$  and the corresponding reference potential-field energy  $E_{\text{pot}}$  are computed, from which the free magnetic energy  $E_{\text{free}} = E_{\text{tot}} - E_{\text{pot}}$  can be derived. The reference potential fields are computed numerically by solving the Laplace equation for the potential with Neumann boundary conditions based on the normal component of  $\mathbf{B}$  on all six boundaries of the analysis volume. As a consequence of each solution field having its own boundary value, there are separate reference potential fields for each of the solution fields, and thus the potential-field energy contents are different among the models. The relative magnetic helicity  $H$  is defined following Berger & Field (1984)

$$H = \int_V (\mathbf{A} + \mathbf{A}_{\text{pot}})(\mathbf{B} - \mathbf{B}_{\text{pot}})dV \quad (16)$$

where  $\mathbf{A}$  is vector potential of the magnetic field, i.e.,  $\mathbf{B} = \nabla \times \mathbf{A}$  and  $\mathbf{B}_{\text{pot}}$  is the reference potential field and also  $\mathbf{B}_{\text{pot}} = \nabla \times \mathbf{A}_{\text{pot}}$ . The calculation of  $H$  is made using a rapid method developed by Valori et al. (2012). For reference, we also list values of the total unsigned magnetic flux  $\Phi$  in the table.

Clearly the free energy increases from NLFFF1 to NLFFF2. Such an increase of non-potentiality of the solutions is due to the improvement of the NLFFF extrapolations. Here the free energy for NLFFF1 is even un-physically negative. We note

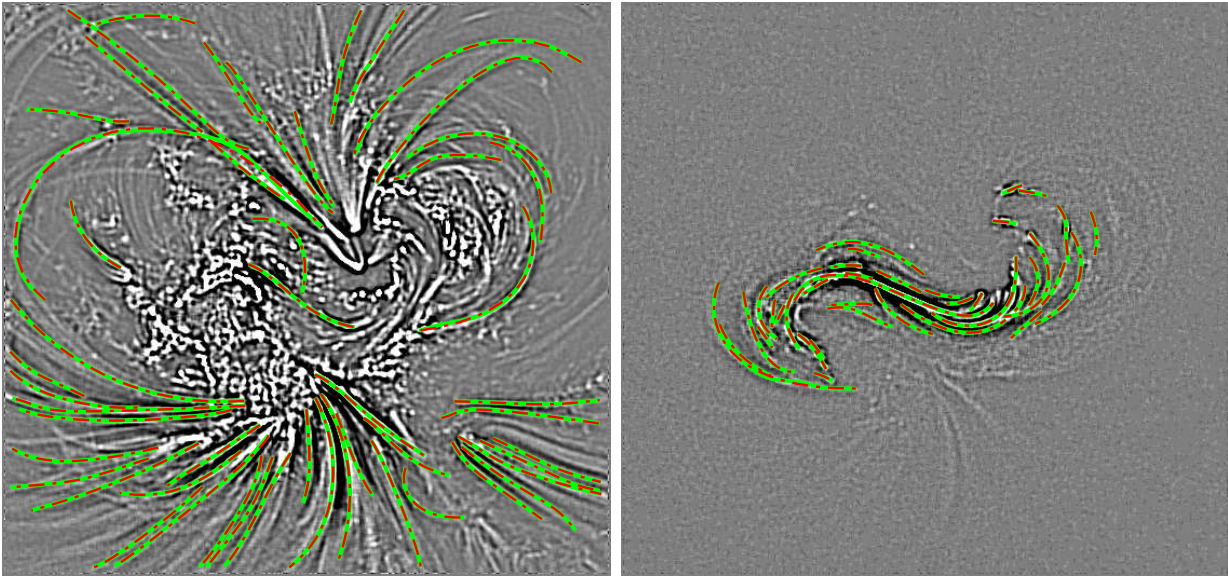


FIG. 4.— Fitting of the OCCULT-2 traced loops (thick green curves) by 2D Bézier splines (dashed red curves). The background are bandpass filtered AIA images, left for AIA 171 Å and right for AIA 94 Å.

that energy of the extrapolated field being lower than the potential field energy has been reported previously, for instance, some solutions given in Table 3 of Metcalf et al. (2008) and Table 1 of Schrijver et al. (2008). Valori et al. (2013) shows that such problematic extrapolation actually reflects the violation of Thomson’s theorem (that the total energy of a system can be expressed as the sum of its potential energy and its free energy) due to the finite divergence of the extrapolation field rather than the non-zero Lorentz force. The finite divergence is unavoidably induced in the course of seeking a force-free field with an inconsistent boundary condition (i.e., the unprocessed photospheric field). Since the MHD-relaxation code attempts to construct force-free solution by reducing the Lorentz forces in the computing volume, while the boundary condition is incompatible with the force-free equation, the reduction of the Lorentz forces is at the expense of the solenoidal condition. In such case, the more inconsistent the boundary is, the higher the divergence of the solution will be, and Thomson’s theorem will be more severely violated, which could result in a total energy lower than the potential energy. The inconsistency of the photospheric field can be partly reduced by preprocessing. After preprocessing, the code outputs free energy on the order of  $10^{32}$  erg, which could energize a major flare. Interestingly, the NFFF model outputs a significantly larger free energy content, which is about three times of that from NLFFF2. This might be due to the fact that NFFF is a combination of LFFFs whose current is distributed more evenly and result in a field much more non-potential than the NLFFFs.

All the models have negative helicity, which complies with the hemispheric chirality-rule (Seehafer 1990; Pevtsov et al. 1995), i.e., active regions in southern and northern hemispheres tend to have negative and positive helicities respectively. A negative helicity indicates a left-handed twisting of the magnetic field lines, and can be easily confirmed by inspecting the magnetic field lines and their directions (see Figure 3) and also in the twist degree map (Figure 3), which shows that the majority of the values is negative. Consistent with the increasing of free energy from NLFFF1, NLFFF2 to NFFF, the relative helicity contents also increase.

## 6. DISCUSSION

Due to the absence of direct measurements, to determine the coronal magnetic field one has to extrapolate the photospheric field. Critically assessing and comparing the results for different extrapolation codes is an important task for developing a reliable coronal magnetic field model consistent with observations and physics. In this paper, we have made a comprehensive assessment and comparison of an NLFFF code (CESE-MHD-NLFFF) and a non-force-free code. For this, we extrapolated the coronal magnetic field for a sigmoidal AR near its central meridian passage immediately before a major flare. Vector magnetograms of the HMI SHARP dataset are used, and three field models are calculated including the CESE-MHD-NLFFF extrapolations using the magnetogram with and without preprocessing and the NFFF extrapolation. The extrapolation solutions are evaluated and compared in different ways including the residual Lorentz force and divergence, the magnetic topology and energy/helicity contents. In particular, we use a method recently proposed by Gary et al. (2014b) to compute the misalignment angle of the model field lines with the 3D traces of coronal loops identified from two AIA images (wave lengths of 94 Å and 171 Å), respectively, which previously have not been tested for these codes.

The extrapolations show that the magnetic field lines in the AR’s core is consistent with sheared arcades forming a sigmoidal shape in agreement with the observed AIA 94 Å loops. Twist of the field lines are mostly below one full turn, and also there seems to be no QSL that marks a clear presence of magnetic flux rope. It is found that the best extrapolated field matches the AIA 94 Å loops with misalignment angles of mean value  $\sim 15^\circ$  and median value  $9^\circ$ , which are much smaller than that for the 171 Å loops (mean value of  $\sim 32^\circ$  and median value of  $\sim 19^\circ$ ). Interestingly, the misalignment angles for AIA 94 Å loops are even comparable with those by coronal-loop forward-fitting method (Aschwanden 2013b), suggesting that the CESE-MHD-NLFFF can reproduce the magnetic configuration at the core region of an AR. On the other hand, the 171 Å loops are not well reproduced,

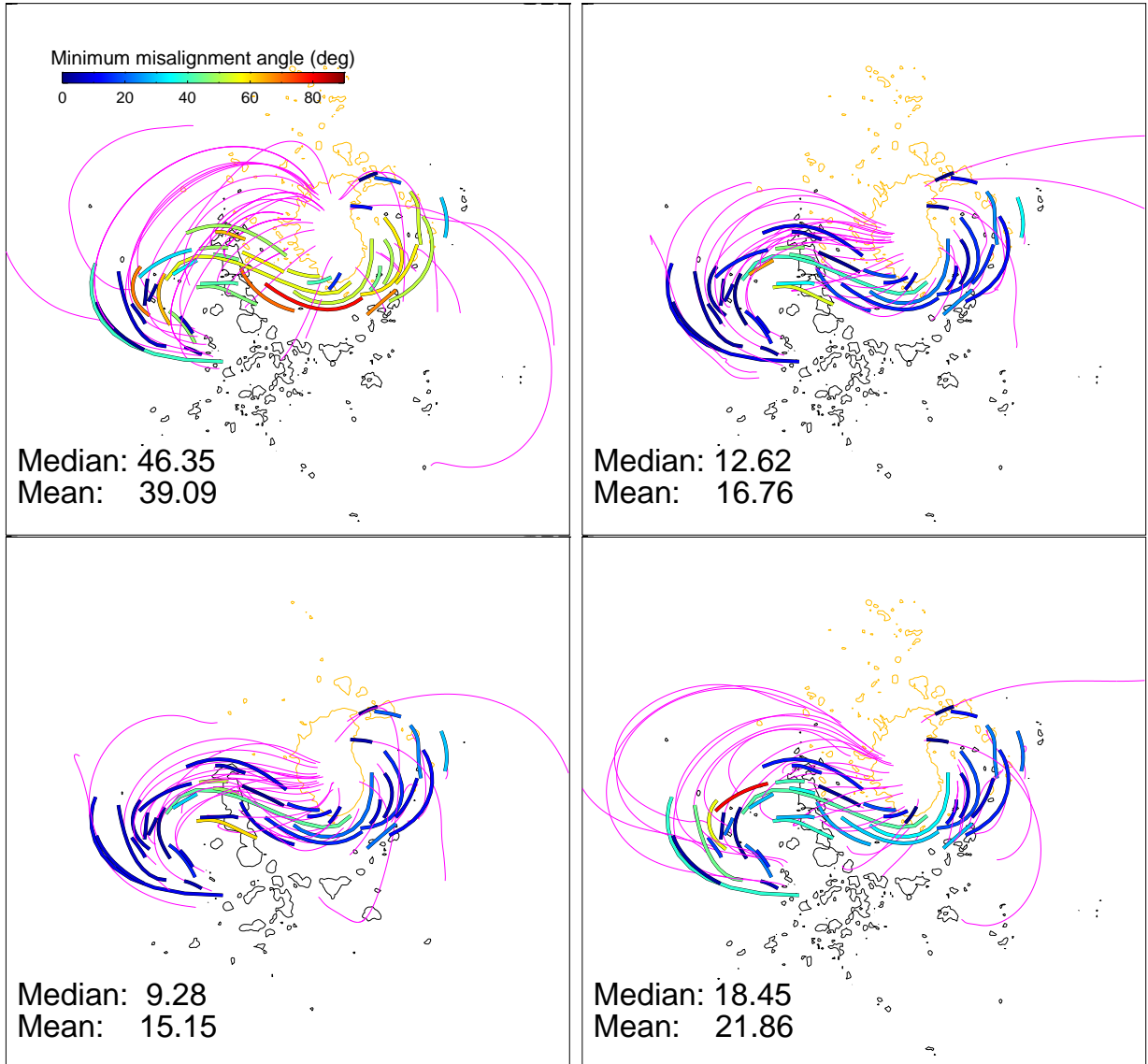


FIG. 5.— Minimum misalignment angles between the magnetic field model and the Bézier splines (for AIA 94 Å loops) when extended to 3D. The four panels clockwise from the top left to the bottom left are results, respectively, for the potential magnetic field, the NLFFF1, the NFFF, and the NLFFF2 models. Each loop, as shown by the thick curves, is color-coded by the value of its misalignment angle ( $0-90^\circ$ ) as indicated by the colorbar in the first panel. Also a magnetic field line (shown by thin curves) is traced from the mid-point of each loop. The contour lines are plotted for  $B_z$  at  $-500$  G (colored as black) and  $500$  G (yellow). For each model, the median and mean values of the misalignment angles for all the loops are shown.

which means that an improvement of the code is necessary for further relaxation of the long field lines. By comparing the NLFFF extrapolations made using both preprocessed and not preprocessed input data, we confirm the preprocessing of vector magnetogram improves considerably the extrapolation result. For the best results, the residual Lorentz force is as large as 15% in normalized units (see above) while the residual divergence is one order of magnitude smaller. When comparing the NLFFFs and the NFFF results, it is found that the currents of the field by the NFFF is distributed more evenly than in the NLFFFs for this particular AR. In the future we plan to extend the comparison study with coronal loops to a number of AR samples, as well as including the magnetic field results from a data-driven MHD model (Jiang et al. 2016). Experiments by using NFFF solutions as initial conditions to MHD

simulations are also underway.

This work is jointly supported by National Natural Science Foundation of China (41604140), China Postdoctoral Science Foundation funded project (119103S277), and the Specialized Research Fund for State Key Laboratories. C.J. acknowledges support by National Natural Science Foundation of China (41531073, 41374176, 41574170, 41231068, and 41574171). Data from observations are courtesy of NASA SDO/AIA and the HMI science teams. We thank the anonymous referee for helpful comments on the manuscript. We were all saddened by the sudden passing of Dr. S. T. Wu. We dedicate this work to ST in memory of his life-long achievement, his mentorship, and his vision for numerical modeling of solar coronal magnetic field.

#### REFERENCES

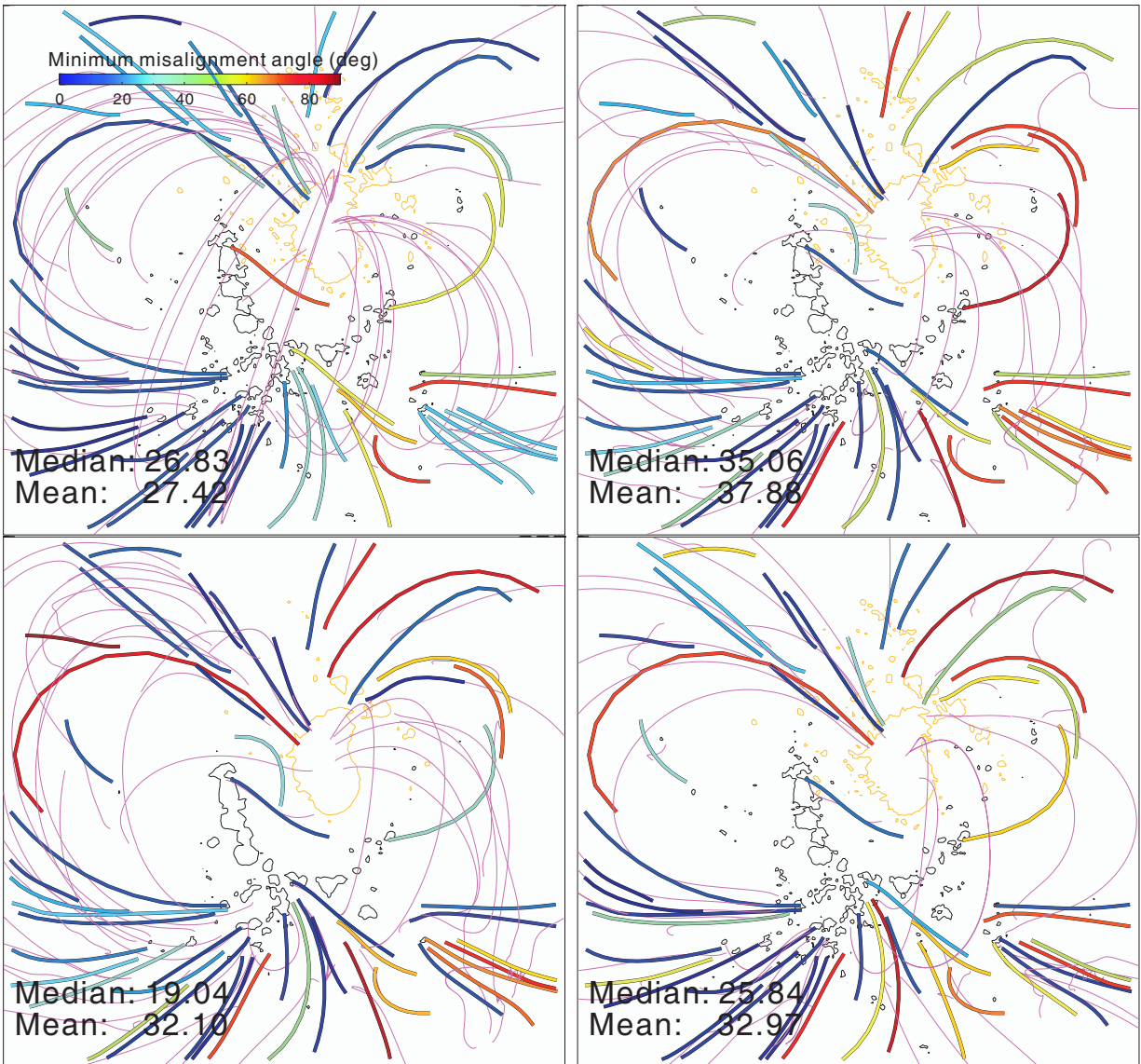


FIG. 6.— Same as Figure 5 but for AIA 171 Å loops.

- Amari, T., Aly, J. J., Luciani, J. F., Boulmezaoud, T. Z., & Mikic, Z. 1997, *Sol. Phys.*, 174, 129
- Amari, T., Boulmezaoud, T. Z., & Aly, J. J. 2006, *A&A*, 446, 691
- Amari, T., Canou, A., & Aly, J. J. 2014, *Nature*, 514, 465
- Aschwanden, M., De Pontieu, B., & Katrukha, E. 2013, *Entropy*, 15, 3007
- Aschwanden, M. J. 2013a, *Sol. Phys.*, 287, 323
- . 2013b, *ApJ*, 763, 115
- Aschwanden, M. J., Sun, X., & Liu, Y. 2014, *The Astrophysical Journal*, 785, 34
- Aschwanden, M. J., Wulser, J.-P., Nitta, N. V., & Lemen, J. R. 2008, *The Astrophysical Journal*, 679, 827
- Aulanier, G., Janvier, M., & Schmieder, B. 2012, *A&A*, 543, A110
- Berger, M. A. & Field, G. B. 1984, *Journal of Fluid Mechanics*, 147, 133
- Berger, M. A. & Prior, C. 2006, *Journal of Physics A Mathematical General*, 39, 8321
- Bobra, M. G., Sun, X., Hoeksema, J. T., Turmon, M., Liu, Y., Hayashi, K., Barnes, G., & Leka, K. D. 2014, *Sol. Phys.*, 289, 3549
- Burnette, A. B., Canfield, R. C., & Pevtsov, A. A. 2004, *ApJ*, 606, 565
- Chae, J. & Moon, Y.-J. 2005, *ApJ*, 629, 1110
- Cheng, X., Ding, M. D., & Fang, C. 2015, *ApJ*, 804, 82
- Cheng, X., Ding, M. D., Zhang, J., Sun, X. D., Guo, Y., Wang, Y. M., Kliem, B., & Deng, Y. Y. 2014, *The Astrophysical Journal*, 789, 93
- Dellar, P. J. 2001, *J. Comput. Phys.*, 172, 392
- Demoulin, P., Henoux, J. C., Priest, E. R., & Mandrini, C. H. 1996, *A&A*, 308, 643
- DeRosa, M. L., Schrijver, C. J., Barnes, G., Leka, K. D., Lites, B. W., Aschwanden, M. J., Amari, T., Canou, A., McTiernan, J. M., Régnier, S., Thalmann, J. K., Valori, G., Wheatland, M. S., Wiegelmann, T., Cheung, M. C. M., Conlon, P. A., Fuhrmann, M., Inhester, B., & Tadesse, T. 2009, *ApJ*, 696, 1780
- DeRosa, M. L., Wheatland, M. S., Leka, K. D., Barnes, G., Amari, T., Canou, A., Gilchrist, S. A., Thalmann, J. K., Valori, G., Wiegelmann, T., Schrijver, C. J., Malanushenko, A., Sun, X., & Régnier, S. 2015, *ApJ*, 811, 107
- Dudík, J., Polito, V., Janvier, M., Mulay, S. M., Karlický, M., Aulanier, G., Del Zanna, G., Džifčáková, E., Mason, H. E., & Schmieder, B. 2016, *The Astrophysical Journal*, 823, 41
- Fuhrmann, M., Seehafer, N., & Valori, G. 2007, *A&A*, 476, 349
- Fuhrmann, M., Seehafer, N., Valori, G., & Wiegelmann, T. 2011, *A&A*, 526, A70
- Gary, G. A. 2001, *Sol. Phys.*, 203, 71
- Gary, G. A., Hu, Q., & Lee, J. K. 2014a, *Sol. Phys.*, 289, 847
- Gary, G. A., Hu, Q., Lee, J. K., & Aschwanden, M. J. 2014b, *Sol. Phys.*, 289, 3703
- Gilchrist, S. A. & Wheatland, M. S. 2014, *Sol. Phys.*, 289, 1153
- Guo, Y., Ding, M. D., Wiegelmann, T., & Li, H. 2008, *ApJ*, 679, 1629
- Guo, Y., Xia, C., Keppens, R., & Valori, G. 2016, *ApJ*, 828, 82
- He, H. & Wang, H. 2006, *MNRAS*, 369, 207
- Hoeksema, J. T., Liu, Y., Hayashi, K., Sun, X., Schou, J., Couvidat, S., Norton, A., Bobra, M., Centeno, R., Leka, K. D., Barnes, G., & Turmon, M. 2014, *Sol. Phys.*, 289, 3483
- Hu, Q. & Dasgupta, B. 2008, *Sol. Phys.*, 247, 87
- Hu, Q., Dasgupta, B., Choudhary, D. P., & Büchner, J. 2008, *ApJ*, 679, 848

- Hu, Q., Dasgupta, B., Derosa, M. L., Büchner, J., & Gary, G. A. 2010, *Journal of Atmospheric and Solar-Terrestrial Physics*, 72, 219
- Inoue, S., Hayashi, K., Magara, T., Choe, G. S., & Park, Y. D. 2014, *The Astrophysical Journal*, 788, 182
- Inoue, S., Kusano, K., Magara, T., Shiota, D., & Yamamoto, T. T. 2011, *ApJ*, 738, 161
- Janvier, M., Aulanier, G., Pariat, E., & Démoulin, P. 2013, *A&A*, 555, A77
- Jiang, C. & Feng, X. 2013, *ApJ*, 769, 144
- , 2014, *Sol. Phys.*, 289, 63
- Jiang, C., Feng, X., & Xiang, C. 2012, *ApJ*, 755, 62
- Jiang, C., Wu, S. T., Feng, X., & Hu, Q. 2014, *ApJ*, 786, L16
- Jiang, C. W. & Feng, X. S. 2012a, *ApJ*, 749, 135
- , 2012b, *Sol. Phys.*, 281, 621
- Jiang, C. W., Feng, X. S., Fan, Y., & Xiang, C. 2011, *ApJ*, 727, 101
- Jiang, C. W., Feng, X. S., Wu, S. T., & Hu, Q. 2013, *ApJ*, 771, L30
- Jiang, C. W., Feng, X. S., Zhang, J., & Zhong, D. K. 2010, *Sol. Phys.*, 267, 463
- Jiang, C. W., Wu, S. T., Feng, X. S., & Hu, Q. 2016, *Nature Comm.*, 7, 11522
- Kliem, B., Su, Y. N., van Ballegooijen, A. A., & DeLuca, E. E. 2013, *ApJ*, 779, 129
- Li, T. & Zhang, J. 2015, *ApJ*, 804, L8
- Lim, E.-K., Jeong, H., Chae, J., & Moon, Y.-J. 2007, *ApJ*, 656, 1167
- Lin, H. 2016, *Frontiers in Astronomy and Space Sciences*, 3, 9
- Lin, H., Kuhn, J. R., & Coulter, R. 2004, *ApJ*, 613, L177
- Liu, C., Deng, N., Lee, J., Wiegelmann, T., Jiang, C., Dennis, B., Su, Y., Donea, A., & Wang, H. 2014, *ApJ*, 795, 128
- Liu, R., Kliem, B., Titov, V. S., Chen, J., Wang, Y., Wang, H., Liu, C., Xu, Y., & Wiegelmann, T. 2016, *ApJ*, 818, 148
- Low, B. C. & Lou, Y. Q. 1990, *ApJ*, 352, 343
- Malanushenko, A., Schrijver, C. J., DeRosa, M. L., & Wheatland, M. S. 2014, *ApJ*, 783, 102
- Malanushenko, A., Schrijver, C. J., DeRosa, M. L., Wheatland, M. S., & Gilchrist, S. A. 2012, *ApJ*, 756, 153
- Malanushenko, A., Yusuf, M. H., & Longcope, D. W. 2011, *ApJ*, 736, 97
- McClymont, A. N., Jiao, L., & Mikic, Z. 1997, *Sol. Phys.*, 174, 191
- Metcalf, T. R., DeRosa, M. L., Schrijver, C. J., Barnes, G., van Ballegooijen, A. A., Wiegelmann, T., Wheatland, M. S., Valori, G., & McTiernan, J. M. 2008, *Sol. Phys.*, 247, 269
- Moore, R. L., Sterling, A. C., Hudson, H. S., & Lemen, J. R. 2001, *ApJ*, 552, 833
- Pariat, E. & Démoulin, P. 2012, *A&A*, 541, A78
- Pevtsov, A. A., Canfield, R. C., & Metcalf, T. R. 1995, *ApJ*, 440, L109
- Quintero, C., Shimizu, T., Katsukawa, Y., de la Cruz Rodríguez, J., Carlsson, M., Anan, T., Oba, T., Ichimoto, K., & Suematsu, Y. 2017, *MNRAS*, 464, 4534
- Régnier, S. 2013, *Solar Physics*, 288, 481
- Sakurai, T. 1981, *Solar physics*, 69, 343
- Sakurai, T. 1982, *Sol. Phys.*, 76, 301
- , 1989, *Space Sci. Rev.*, 51, 11
- Schrijver, C. J., De Rosa, M. L., Metcalf, T. R., Liu, Y., McTiernan, J., Régnier, S., Valori, G., Wheatland, M. S., & Wiegelmann, T. 2006, *Sol. Phys.*, 235, 161
- Schrijver, C. J., DeRosa, M. L., Metcalf, T., Barnes, G., Lites, B., Tarbell, T., McTiernan, J., Valori, G., Wiegelmann, T., Wheatland, M. S., Amari, T., Aulanier, G., Démoulin, P., Fuhrmann, M., Kusano, K., Régnier, S., & Thalmann, J. K. 2008, *ApJ*, 675, 1637
- Seehafer, N. 1978, *Sol. Phys.*, 58, 215
- , 1990, *Sol. Phys.*, 125, 219
- Snyder, J. P. 1987, *Map projections—A working manual*, Vol. 1395 (US Government Printing Office)
- Solanki, S. K., Inhester, B., & Schüssler, M. 2006, *Reports on Progress in Physics*, 69, 563
- Sun, X., Hoeksema, J. T., Liu, Y., Wiegelmann, T., Hayashi, K., Chen, Q., & Thalmann, J. 2012, *ApJ*, 748, 77
- Tadesse, T., Wiegelmann, T., MacNeice, P., Inhester, B., Olson, K., & Pevtsov, A. 2014, *Solar Physics*, 289, 831
- Titov, V. S. & Démoulin, P. 1999, *A&A*, 351, 707
- Titov, V. S., Hornig, G., & Démoulin, P. 2002, *J. Geophys. Res.*, 107, 1164
- Valori, G., Démoulin, P., Pariat, E., & Masson, S. 2013, *A&A*, 553, A38
- Valori, G., Green, L. M., Démoulin, P., Vargas Domínguez, S., van Driel-Gesztelyi, L., Wallace, A., Baker, D., & Fuhrmann, M. 2012, *Sol. Phys.*, 278, 73
- Valori, G., Kliem, B., & Fuhrmann, M. 2007, *Sol. Phys.*, 245, 263
- Valori, G., Kliem, B., Török, T., & Titov, V. S. 2010, *A&A*, 519, A44+
- Wheatland, M. S. 2006, *Sol. Phys.*, 238, 29
- , 2007, *Sol. Phys.*, 245, 251
- Wheatland, M. S., Sturrock, P. A., & Roumeliotis, G. 2000, *ApJ*, 540, 1150
- Wiegelmann, T. 2004, *Sol. Phys.*, 219, 87
- , 2008, *Journal of Geophysical Research (Space Physics)*, 113, 3
- Wiegelmann, T. & Neukirch, T. 2002, *Sol. Phys.*, 208, 233
- , 2006, *A&A*, 457, 1053
- Wiegelmann, T. & Sakurai, T. 2012, *Living Reviews in Solar Physics*, 9, 5
- Wiegelmann, T., Thalmann, J. K., Inhester, B., Tadesse, T., Sun, X., & Hoeksema, J. T. 2012, *Sol. Phys.*, 67
- Wu, S. T., Sun, M. T., Chang, H. M., Hagyard, M. J., & Gary, G. A. 1990, *ApJ*, 362, 698
- Xue, Z., Yan, X., Cheng, X., Yang, L., Su, Y., Kliem, B., Zhang, J., Liu, Z., Bi, Y., Xiang, Y., et al. 2016, *Nature Communications*, 7
- Yan, Y. & Sakurai, T. 2000, *Sol. Phys.*, 195, 89
- Yang, W. H., Sturrock, P. A., & Antiochos, S. K. 1986, *ApJ*, 309, 383
- Zhao, J., Gilchrist, S. A., Aulanier, G., Schmieder, B., Pariat, E., & Li, H. 2016, *ApJ*, 823, 62